RSC Advances

ROYAL SOCIETY OF CHEMISTRY

www.rsc.org/advances

Solution Processable Star-Shaped Molecules with a Triazine Core and Branching Thienylenevinylenes for Bulk Heterojunction Solar Cells

Chien-Yi Huang, Wan-Hua Lee, and Rong-Ho Lee*

Department of Chemical Engineering, National Chung Hsing University, Taichung, 402, Taiwan

*To whom correspondence should be addressed.

Rong-Ho Lee—e-mail: rhl@dragon.nchu.edu.tw; tel.: +886-4-22854308; fax: +886-4-22854734.

Abstract

Two new star-shaped A-π-D molecules with triazine as a core and an acceptor unit, thienylenevinylene as the π bridge, and *tert*-butyl-substituted triphenylamine (*t*TPA)- or carbazole (*t*Cz) as the end group and donor units of TTVTPA and TTVCz were synthesized for the application as donor materials in solution processed bulk heterojunction organic solar cells (OSCs). The charge transfer was convergent from peripheral groups to the central core along the conjugated branches in these star-shaped molecules (SSMs). TTVTPA and TTVCz are soluble in common organic solvents. Excellent thermal stability was observed for TTVTPA and TTVCz. OSCs were fabricated by spin-coating a blend of each SSM with the fullerene derivatives ($PC_{61}BM$ or $PC_{71}BM$) as a composite film-type photoactive layer. The PV properties of the TTVTPA/fullerene derivative based OSCs were much better than those of the TTVCz/fullerene derivative blend based OSCs. A power conversion efficiency of 2.48 %, a short-circuit current density of 10.57 mA/cm^2, an open-circuit voltage of 0.69 V, and a fill factor of 0.34 were observed for the OSC based on the active layer of TTVTPA/$PC_{71}BM$ (1:7, w/w).

Keywords: triphenylamine, carbazole, thiophenevinylene, photovoltaic performance, bulk heterojunction cell.

1. Introduction

The bulk heterojunction (BHJ) type organic solar cells (OSCs) based on the blend of organic semiconductors and fullerene derivatives have been widely studied [1]. OSCs have many unique advantages, such as light weight, low cost, flexible device and large-scale production capability. In particular, the solution processable small molecules for use in BHJ type OSCs application have attracted much attention in recent years, because of their unique advantages of well-defined structure, easy purification, definite molecular weight, easy mass-scale production and good batch to batch reproducibility [2-4]. Many efforts have been made to develop small molecules for OSC applications, including the linear molecules [5-10], star shaped-molecules (SSMs) [11], X-shaped molecules [12-13], and dendritic molecules [14-15].

SSMs have been developed as a photo-energy conversion material for OSC due to a numbers of advantages [16-34]. By tailoring the functional groups in the core, the bridge, and end groups, SSMs can be designed to realize high mobilities, small band gaps and broad absorptions in the visible region in OSCs, resulting in an improvement of the photo-energy conversion efficiency (PCE) [16-31]. Many electron donor-π conjugated-acceptor (D-π-A) structured SSMs based on triphenylamine (TPA) core derivatized with various conjugated bridges and electron-withdrawing groups have been investigated [16-27,34]. SSM with D-π-A structure exhibits a low band gap and broad absorption in the visible region due to the intramolecular charge transfer (ICT), an easily tuned energy level and band gap through adjusting the donor and acceptor units, and π-bridge units or length [16-18]. In addition, the TPA cored SSMs with electron-acceptor dicyanovinyl (DCN) as end groups have been studied by several researchers [16, 19, 20]. Introduction of the DCN group induces a shift of the absorption onset toward longer wavelengths and an

increase of the open circuit voltage (V_{OC}) under solar light illumination, resulting in the improved PCE of OSCs [16]. A high V_{OC} value (1.07 V) was observed for an OSC based on the unsymmetrical TPA cored SSM [21]. The incorporation of two DCN groups as the end group leads to a broad absorption, high absorption coefficient, and low lying HOMO level, resulting in the high V_{OC} of such SSM based OSCs. The TPA cored SSMs with different conjugated bridges (4,4'-dihexyl-2,2'-bithiophene (bT) and 4,4'-dihexyl-2,2'-bithiophene vinylene (bTV)) for OSCs have also been reported [22]. The OSC based on SSM with bTV bridges exhibits a broader absorption band and higher PCE than the one based on the SSM with bT bridges. In addition, photovoltaic (PV) performances of OSC based on the TPA cored SSM with D-A-D conjugated branches have been studied [23-27,32,33]. The electron-acceptor benzothiadiazole or dialkylated diketopyrrolopyrrole (DPP) has been incorporated as the bridge of the SSM with D-A-D conjugated branches [23-27,32,33]. The incorporation of the bulky group DPP as the acceptor in the conjugated branches may prevent the formation of an ordered, long range and coplanar π-π stacking, which could be beneficial to charge transport across the thin-film based OSC [23]

Another alternative, the trithienobenzene cored planarized SSMs for photoactive layer of OSCs, has been reported in several literature [23]. Roncali et al. reported that incorporating the planar core could reduce the dihedral angle between the core and the branches of SSM. The combined effects of planarization and rigidification of the trithienobenzene core leads to a significant enhancement of π-electron delocalization associated with a decrease of the energy gap for the SSMs [28,29]. Moreover, the SSM with planar core appear to adopt a preferential horizontal orientation on the surface of substrate, which is more favorable for efficient absorption of the incident light. This horizontal orientation behavior associated with the enhanced π-electron delocalization inherent to the fused trithienobenzene lead to a

considerable improvement in performance of the resulting OSC [29]. In addition to the trithienobenzene cored planarized SSMs, the triindole and isotruxene cored SSMs for OSCs have also been reported [30,31]. Such SSMs with a strong electron-donating core exhibit an intensive absorption in a broad region, and relatively high hole mobility. [30]. Despite the fact that the highest PCEs (5-7%) of the solution processable small molecules based BHJ type OSCs has been reported, the relatively low PCE is still a hindrance to their application [4-8,10]. The PV performances of the SSMs with different central cores, conjugated bridges, and periphery groups have not been thoroughly investigated.

As mentioned above, SSMs with an electron-donating core have been extensively studied, including the TPA, trithienobenzene, triindole, and isotruxene cores [16-34]. For these D-π-A structured SSMs, the direction of the dipole moments is divergent from the central core to the peripheral groups along the conjugated branches (Figure 1(a)). In this study, two new solution processable A-π-D structured SSMs with triazine as the core and acceptor unit, thienylenevinylene as the π bridge, and *tert*-butyl-substituted triphenylamine (*t*TPA)- or carbazole (*t*Cz) as the end group and donor units of TTVTPA and TTVCz were synthesized for the application as donor materials in solution processed BHJ type OSCs. The direction of the dipole moments is convergent from the peripheral groups to the central core along the conjugated branches (Figure 1(b)). The incorporation of the electron deficient triazine group as the core decreases the LUMO level and energy gap of the SSM, which is favorable for the harvesting of large amounts of solar radiation. Moreover, the convergence of the dipole moments from the peripheral groups to the central core along the conjugated branches could avoid the formation of a long-ranged and coplanar π-π stacking. This is beneficial to the charge transport across the thin-film based OSC [23]. UV–Vis absorption spectroscopy and cyclic voltammetry

(CV) were used to study the chemical structure effect on the photophysical and electrochemical properties of the SSMs. The BHJ type OSCs based on the photoactive layer of SSM/fullerene derivative ($PC_{61}BM$ or $PC_{71}BM$) blend films were fabricated. The mechanism of charge separation and transfer from the SSM to the fullerene derivatives was proposed, as shown in Figure 2. The charges transfer from the triazine core of SSM to the fullerene derivatives formed channels. We also used atomic force microscopy (AFM) and transmission electron microscopy (TEM) to study the morphology of thin films prepared from SSM (TTVTPA and TTVCz)/$PC_{61}BM$ (or $PC_{71}BM$) blends. We then fabricated OSCs having a conventional indium tin oxide (ITO)-coated glass/hole-transporting medium (HTM)/photoactive layer/Ca (10 nm)/Al (100 nm) structure via spin-coating a blend of each SSM with $PC_{61}BM$ or $PC_{71}BM$ to form a composite film-type photoactive layer on an HTM layer deposited on ITO-coated glass. The PV performance of each of these OSCs was evaluated, and, based on the result, we considered the influence of the molecular-structural features of our A-π-D structured SSMs on OSC performance.

2. Experimental Details

2.1 Chemicals

2-Bromothiophene, paraformaldehyde, n-butyllithium (2.5 M in hexane), and other reagents and chemicals were purchased from Aldrich, Alfa and TCI Chemical Co., and used as received. Dichloromethane (DCM), tetrahydrofuran (THF), dimethylformamide (DMF), toluene, and *o*-dichlorobenzene (*o*-DCB) were freshly distilled over the appropriate drying agents prior to use as solvents, and then were purged with nitrogen. The compounds of diethyl(2-bromothiophen-5-yl)methylphosphonate (1), (E)-4-(5-(2-(2-bromothiophen-5-yl)vinyl)thiophen-2-yl)-N,N-((4,40-di-tert-butyl)diph enyl)aniline (3),

3,6-di-tert-butyl-9-(4-((E)-4-(5-(2-(2-bromothiophen-5-yl)vinyl)thiophen-2-yl))phenyl)carbazole (5), and 2,4,6-tris(4-(4,4,5,5-tetramethyl-1,3,2-dioxaborolan-2-yl) phenyl)-[1,3,5] triazine (7) were synthesized as shown in **Scheme 1**. The syntheses of SSMs (TTVTPA and TTVCz) are illustrated in **Scheme 2**. The compounds of 5-(4-(Bis(4-tert-butylphenyl)amino)phenyl)thiophene-2-carbaldehyde (2), 5-(4-(3,6-Di-tert-9-carbazolyl)phenyl)thiophene-2-carbaldehyde (4), and 2,4,6-tris-(4-bromophenyl)-[1,3,5] triazine (6) were synthesized according to the procedures in the literature [31,35].

Synthesis of compound 1

Compounds 2-bromothiophene (0.96 mL, 10 mmol), paraformaldehyde (0.36 g, 12 mmol), HOAc (20 mL), and HBr (33%, 20 mL) were placed into a flask and heated to 50 ^{o}C for 3 h. The mixture was partitioned between DCM and water, and then the organic phase was dried ($MgSO_4$), filtered, and evaporated to dryness to obtain a red oil (2.0 g, yield = 70 %). The red oil (2.0 g) and phosphorous acid triethyl ester (1.4 mL, 8 mmol) were placed into a flask and heated to 150 ^{o}C for 12 h. Next, the excessive phosphorous acid triethyl ester was removed under vacuum. The crude product was purified by column chromatography on a silica gel with ethyl acetate (EA): n-hexane (1:2) as the eluant to give a yellow oil (compound 1) (3.25 g, yield = 83%). ^{1}H-NMR (δ/ppm, 600 MHz, $CDCl_3$, TMS): 1.30 (t, J = 7.2 Hz, 6H), 3.26 (d, J = 21.0 Hz, 2H), 4.08 (q, J = 5.0 Hz, 4H), 6.73 (d, J = 3.6 Hz, 1H), 6.89 (d, J = 4.2 Hz, 1H). Anal. Calcd for $C_9H_{14}BrPO_3$: C, 38.43; H, 4.98; O, 17.08. Found: C, 38.46; H, 4.94; O, 17.15.

Synthesis of compound 3

A solution of compound 1 (3.44 g, 11 mmol) in DMF (20 mL) was stirred in an ice-water bath for several minutes, and then sodium methoxide (1.62 g, 30 mmol) in DMF (20 mL) was added dropwise. After 20 min, the reaction solution turned

brown. Next, a solution of compound 2 (4.67 g, 10 mmol) in DMF (20 mL) was added dropwise. The mixture was warmed to room temperature and stirred for 5 h, and then MeOH was added to quench the reaction. The crude product was partitioned between DCM and water, and the organic phase was dried ($MgSO_4$), filtered, and evaporated to dryness. The residue was purified by column chromatography on a silica gel with n-hexane as the eluant to give a yellow solid (compound 3) (5.4 g, yield = 86 %). ^{1}H NMR (δ/ppm, 600 MHz, $CDCl_3$, TMS): 1.30 (s, 18H), 6.73-6.75 (d, J = 3.6 Hz, 1H), 6.85-6.87 (d, J = 2.4 Hz, 2H), 6.91-6.92 (d, J = 3.6 Hz, 1H), 6.94-6.96 (d, J = 4.2 Hz, 1H), 7.00-7.04 (m, 6H), 7.06-7.08 (d, J = 4.2 Hz, 1H), 7.23-7.27 (d, J = 6.0 Hz, 4H), 7.39-7.42 (d, J = 8.4 Hz, 2H). Anal. Calcd for $C_{36}H_{36}NS_2Br$: C, 69.00; H, 5.75; N, 2.24; S, 10.22. Found: C, 69.09; H, 5.68; N, 2.32; S, 10.30.

Synthesis of compound 5

A solution of compound 1 (3.14 g, 10 mmol) in DMF (20 mL) was stirred in an ice-water bath for several minutes, and then sodium methoxide (1.62 g, 30 mmol) in DMF (20 mL) was added dropwise. After 20 min, the reaction solution turned brown. Next, a solution of compound 4 (5.12 g, 11 mmol) in DMF (20 mL) was added dropwise. The mixture was warmed to room temperature and stirred for 5 h, and then MeOH was added to quench the reaction. The crude product was partitioned between DCM and water, and the organic phase was dried ($MgSO_4$), filtered, and evaporated to dryness. The residue was purified by column chromatography on a silica gel with DCM: n-hexane (1:10) as the eluant to give a yellow solid (compound 5) (4.1 g, yield = 65.6 %). ^{1}H NMR (δ/ppm, 600 MHz, $CDCl_3$, TMS): 1.45 (s, 18H), 6.78-6.80 (d, J = 6.0 Hz, 1H), 6.91-6.96 (m, 3H), 7.02-7.06 (d, J = 6.6 Hz, 1H), 7.26-7.30 (d, J = 6.0 Hz, 1H), 7.36-7.38 (d, J = 13.2 Hz, 2H), 7.42-7.46 (dd, J = 7.8 Hz, 2H), 7.53-7.56 (d, J = 13.2 Hz, 2H), 7.75-7.80 (d, J =

13.2 Hz, 2H), 8.10-8.12 (s, 2H). Anal. Calcd for $C_{36}H_{34}NS_2Br$: C, 69.23; H, 5.45; N, 2.24; S, 10.26. Found: C, 69.12; H, 5.56; N, 2.19; S, 10.35.

Synthesis of compound 7

A solution of compound 6 (5.42 g, 10 mmol) in dry THF (40 mL) was stirred at -78 ^oC under N_2 for 20 min and then n-BuLi (2.5 M in hexane, 14.0 mL, 35.0 mmol) was added dropwise. The mixture was maintained at -78 ^oC with continued stirring for a further 3 h, at which point a solution of 2-isopropoxy-4,4,5,5-tertamethyl-1,3,5-dioxaborolane (7.14 g, 35 mmol) in THF (10 mL) was added dropwise. After warming to room temperature and stirring for 12 h, MeOH was added to quench the reaction. The solution was partitioned between EA and water; the organic phase was collected, dried ($MgSO_4$), filtered, and evaporated to dryness. The residue was recrystallized (MeOH) to provide a white solid (compound 7) (3.22 g, yield = 47%). ^1H NMR (δ/ppm, 600 MHz, $CDCl_3$, TMS): 1.34 (s, 36H), 7.59-7.63 (d, J = 7.8 Hz, 6H), 7.84-7.88 (d, J = 8.4 Hz, 6H). Anal. Calcd for $C_{39}H_{48}N_3B_3O_6$: C, 68.18; H, 6.99; N, 6.12; O, 13.98. Found: C, 68.21; H, 6.91; N, 6.06; O, 14.05.

Synthesis of TTVTPA

Compound 3 (2.51 g, 4 mmol), compound 7 (0.687 g, 1 mmol), and tetrakis(triphenylphosphine) palladium (0) ($Pd(PPh_3)_4$, 0.05 g, 0.04 mmol) were dissolved in a mixture of toluene and aqueous K_2CO_3 (2 M, 8 mL). The solution was refluxed with vigorous stirring under a nitrogen atmosphere for 48 h. After cooling to room temperature, the solution was partitioned between DCM and water. The organic phase was collected, dried ($MgSO_4$), filtered, and evaporated to dryness. The crude product was purified by column chromatography on a silica gel with DCM: n-hexane (1:10) as the eluant to give a red solid (compound TTVTPA) (0.61 g, yield = 31.1 %). ^1H NMR (δ/ppm, 600 MHz, $CDCl_3$, TMS): 1.29 (s, 54H), 6.90-6.92 (d, J =

4.2 Hz, 3H), 6.93-6.95 (d, *J* = 4.8 Hz, 6H), 6.95-6.97 (d, *J* = 4.2 Hz, 3H), 7.01-7.05 (m, 18H), 7.07-7.09 (d, *J* = 4.2 Hz, 6H), 7.24-7.27 (m, 18H), 7.40-7.43 (m, 12H). ^{13}C NMR (MHz, $CDCl_3$): δ 147.8, 146.1, 144.6, 143.5, 143.4, 143.2, 142.6, 142.3, 141.7, 140.6, 135.9, 128.8, 127.7, 127.6, 127.5, 127.2, 127.0, 126.9, 126.2, 126.1, 126.0, 125.8, 124.3, 122.6, 122.5, 122.4, 121.8, 121.7, 120.8, 120.5, 34.3, 31.4, 30.2, 29.7. Anal. Calcd for $C_{129}H_{120}N_6S_6$: C, 79.63; H, 6.17; N, 4.32. Found: C, 79.57; H, 6.23; N, 4.30.

Synthesis of TTVCz

Compound 5 (2.50 g, 4 mmol), compound 7 (0.687 g, 1 mmol), and tetrakis(triphenylphosphine) palladium (0) ($Pd(PPh_3)_4$, 0.05 g, 0.04 mmol) were dissolved in a mixture of toluene and aqueous K_2CO_3 (2 M, 8 mL). The solution was refluxed with vigorous stirring under a nitrogen atmosphere for 48 h. After cooling to room temperature, the solution was partitioned between DCM and water. The organic phase was collected, dried ($MgSO_4$), filtered, and evaporated to dryness. The crude product was purified by column chromatography on silica gel with DCM: n-hexane (1:10) as the eluant to give an orange solid (compound TTVCz) (0.59 g, yield = 30.2 %). ^{1}H NMR (δ/ppm, 600 MHz, $CDCl_3$, TMS): 1.45 (s, 54H), 7.04-7.08 (m, 9H), 7.27-7.29 (d, J = 4.2 Hz, 3H), 7.29-7.31 (d, *J* = 3.0 Hz, 3H), 7.37-7.42 (m, 9H), 7.44-7.48 (d, J = 8.4 Hz, 6H), 7.55-7.58 (d, *J* = 8.4 Hz, 6H), 7.64-7.68 (d, *J* = 8.4 Hz, 6H), 7.68-7.71 (d, *J* = 7.8 Hz, 6H), 7.77-7.81 (d, *J* = 8.4 Hz, 6H), 8.12 (s, 6H). ^{13}C NMR (MHz, $CDCl_3$): δ 143.0, 142.7, 142.2, 142.0, 139.4, 139.0, 138.3, 137.4, 136.2, 133.3, 132.7, 130.3, 127.7, 127.6, 127.5, 127.3, 127.0, 126.8, 126.5, 126.0, 124.3, 124.1, 123.9, 123.7, 123.5, 121.6, 121.4, 116.3, 109.2, 34.7, 32.0. Anal. Calcd for $C_{129}H_{144}N_6S_6$: C, 78.66; H, 7.32; N, 4.27. Found: C, 78.59; H, 7.30; N, 4.29.

2.2 Characterization of Copolymers

^{1}H NMR (600 MHz) spectra were recorded using a Varian Unity Inova spectrometer. Elemental analysis was performed using an elemental analyzer (Elementar Vario EL III). The glass transition temperature (T_g) and thermal decomposition temperature (T_d; temperature at which weight loss reaches 5%) of the SSMs were determined by means of differential scanning calorimetry (TA Instruments, DSC-2010) and thermogravimetric analysis (TA Instruments, TGA-2050), respectively. Both analyses were performed under a N_2 atmosphere at a scanning (both heating and cooling) rate of 10 °C min^{-1}. The temperatures at the intercepts of the curves in the thermogram (endothermic, exothermic, or weight loss) with the leading baseline were taken as estimates of T_g and T_d. The absorption spectra were measured using a Hewlett-Packard 8453 UV–Vis spectrometer. The fluorescence spectra were measured using an Acton Research Spectra Pro-150 luminescence spectrometer. Dilute *o*-DCB solutions of the TTVTPA and TTVCz s were filtered through a 0.45-μm filter to remove the insoluble materials before spectral measurements. The redox potentials of the TTVTPA and TTVCz were determined using a CHI 611D electrochemical analyzer (scanning rate: 50 mV s^{-1}) equipped with Pt electrodes and an Ag/Ag$^+$ (0.10 M $AgNO_3$ in MeCN) reference electrode in an anhydrous, N_2-saturated solution of 0.1 M Bu_4NClO_4 in MeCN. A Pt plate coated with a thin polymer film was used as the working electrode; a Pt wire and an Ag/Ag$^+$ electrode were used as the counter and reference electrodes, respectively. The electrochemical potential was calibrated against ferrocene/ferrocenium. The morphology of films prepared from TTVTPA/$PC_{61}BM$ and TTVCz/$PC_{61}BM$ blends was studied using an atomic force microscope (AFM, Seiko SII SPA400) operated in the tapping mode and using a transmission electron microscope (TEM, JEOL JEM-1400).

2.3 Fabrication and Characterization of the OSCs

The OSCs fabricated in this study had an indium tin oxide (ITO)-coated glass /

hole-transporting material (HTM) / photoactive layer / Ca (10 nm) / Al (100 nm) structure, in which the photoactive layer consisted of an interpenetrating network of SSM and the fullerene derivative $PC_{61}BM$ or $PC_{71}BM$. The ITO-coated glass (sheet resistance: 20 Ω square^{-1}) was purchased from Applied Film Corp. $PC_{61}BM$ and $PC_{71}BM$ were purchased from American Dye Source and used as received. The OSCs were fabricated as follows: glass substrates with patterned ITO electrodes were washed well, and then cleaned by means of O_2 plasma treatment. A thin film of the HTM, poly(3,4-ethylenedioxythiophene) doped with poly(styrene sulfonate) (PEDOT:PSS, AI4083, Heraeus Clevios GmbH), was deposited onto the ITO layer using the spin-casting method. The sample was dried at 150°C for 30 min in a glove box. A mixture solution of SSM and fullerene derivative $PC_{61}BM$ or $PC_{71}BM$ (30 mg/mL in o-DCB) was stirred overnight, and then filtered through a 0.2-μm poly(tetrafluoroethylene) (PTFE) filter and spin-coated (1500 rpm, 30 s) onto the HTM layer to prepare the SSM/$PC_{61}BM$ (or SSM/$PC_{71}BM$) composite film-based photo-active layer. The sample was dried at 80 °C for 60 min in a glove box. In a high-vacuum chamber, the Ca/Al-based cathode was thermally deposited onto the SSM/$PC_{61}BM$ (or SSM/$PC_{71}BM$) composite layer. The active area of the OSC was 0.04 cm2. After electrode deposition, the OSC was encapsulated. The cathode deposition rate was determined using a quartz thickness monitor (STM-100/MF, Sycon). The thickness of the thin films was determined using a surface texture analysis system (3030ST, Dektak). The PV properties of the OSCs were measured using a programmable electrometer equipped with current and voltage sources (Keithley 2400) under illumination with solar-simulating light (100 mW cm^{-2}) from an AM1.5 solar simulator (NewPort Oriel 96000).

3. Results and Discussion

3.1. Characterization of SSMs

Chemical structures of the SSMs (TTVTPA and TTVCz) were confirmed by 1H NMR spectroscopy and using an elemental analyzer. SSMs were soluble in common organic solvents, including cyclohexanone, toluene, xylene, dichloromethane, chloroform, THF, and *o*-DCB. Excellent solubility is favorable for the solution processing of the SSMs based photo-active layer. However, the operational stability of OSCs is directly related to the thermal stability of the component conjugated SSM. Thus, high values of T_g and T_d are desirable. We measured the T_g and T_d of two SSMs by means of thermal analyses using DSC and TGA, as shown in Figure S1(a) and Figure S1(b) (supporting information), respectively. The transition temperatures were determined from the second round of the DSC heating scans. The values of T_g for TTVTPA and TTVCz were 135.8 ℃ and 168.6 ℃, respectively. A higher T_g value was observed for the TTVCz compared to the TTVTPA. The reason for this difference may be that the propeller-shaped conformation of the TPA moiety is expected to increase the free volume between the SSMs, while the coplanar structure of carbazole permits a higher packing density [37]. In addition, the values of T_d for TTVTPA and TTVCz were 432.2 and 428.4 ℃, respectively. The high thermal stabilities of TTVTPA and TTVCz are suitable for OSC applications.

3.2 Optical properties of the SSMs

UV-vis absorption spectra of the SSMs (TTVTPA and TTVCz) in *o*-DCB solution and as solid films are shown in Fig 3. Table 1 summarizes the photophysical properties of the SSMs. As shown in Fig 3, the absorption bands of TTVTPA and TTVCz in *o*-DCB ranged from 350 to 575 nm, and each conjugated molecule exhibited a broad absorption band. The maximum absorption wavelengths of TTVTPA and TTVCz in *o*-DCB were at 495 nm and 442 nm, respectively, representing the intramolecular charge transfer (ICT) transitions between the triazine

core and the conjugated branches. The red-shift of the absorption band for TTVTPA relative to TTVCz should be due to the stronger electron-donating character and more efficient π-π* charge transfer of *t*TPA terminated branches. In addition, the absorption bands of TTVTPA and TTVCz thin films ranged from 350 to 625 nm. The maximum absorption wavelengths of TTVTPA and TTVCz as thin films were at 488 nm and 446 nm, respectively. The absorption bands of TTVTPA and TTVCz in thin film form were not red-shifted compared to those of the ones in *o*-DCB. This behavior is closely related to the molecular packing of SSMs in the solid state [29]. The result indicated that a long range π-π stacking was not present in the thin film state for the A-π-D structured SSMs (TTVTPA and TTVCz). Most of the D-π-A or D-π-D structured SSMs exhibit a red-shift of the maximum absorption wavelengths in the thin-film state in comparison with that of the ones in the solution state [19, 27, 29]. Nevertheless, the onset wavelength of the absorption band was increased for the SSMs in the thin-film state compared to the ones in solution state, especially for the TTVCz. In addition, the full widths at half-maximum (FWHM) of the absorption bands of the TTVTPA and TTVCz in the films were greater than those in solution, presumably because of the conformation of the SSMs in the thin-film state was more complex compared to the ones in solution state. As a result, larger FWHM values were observed for the SSMs in the thin-film state.

In addition, we determined the band-gap energies (E_g) of the SSMs in the thin film state from the onset wavelengths of their absorption bands. As presented in Table 1, the values of E_g for TTVTPA and TTVCz were 2.05 eV and 2.09 eV, respectively. The lower value of E_g should reflect a higher amount of charge transfer between the triazine core and the conjugated branches for the TTVTPA compared to the TTVCz. Generally, the broader absorption and lower band-gap energy characteristics are expected to improve the solar-light absorption efficiency of the

photo-energy conversion layer in OSCs, resulting in greater photocurrent generation.

3.3 Electrochemical properties of SSMs

Because the PV performance of OSC is related to the electro-chemical behavior of the SSM, we used cyclic voltammetry to investigate the electrochemical behavior of the SSMs and to estimate the energy levels of the highest occupied molecular orbital (HOMO). The oxidation behaviors in the CV curves of the SSMs TTVTPA and TTVCz are shown in Fig 4. The electrochemical properties of the TTVTPA and TTVCz are summarized in Table 1. The oxidation potentials (E_{on}^{ox}) of TTVTPA and TTVCz were 0.76 V and 0.87 V, respectively. From those values, the HOMO levels of the SSMs were calculated according to the following equation:

$$\text{HOMO} = -\text{e}(E_{on}^{ox} - E_{on,\ \text{ferrocene}}^{ox} + 4.8)\ (\text{eV})$$

where 4.80 eV is the energy level of ferrocene below the vacuum level, and the E_{on}^{ox} of ferrocene/ferrocene^{+} is 0.09 V in 0.1 M Bu_4NClO_4/MeCN solution. The HOMO levels were obtained as -5.47 and -5.58 eV for TTVTPA and TTVCz, respectively. The HOMO level of TTVTPA is higher than that of TTVCz. It is also known that attachment of *tert*-butyl groups on electrochemically active sites of aromatic amines leads to a decrease of the HOMO level [38]. Here, *t*Cz terminated SSM (TTVCz) exhibited a lower HOMO level than that of the *t*TPA terminated SSM (TTVTPA), presumably because of the larger oxidation potential and weaker electron-donating ability of carbazole derivatives [39]. In general, the HOMO energy level of a p-type conjugated molecule is an important parameter that affects the performance of BHJ-type cells. High V_{OC} value is typically obtained for OSCs fabricated from SSMs with low HOMO energy levels [40]. Because no reversible n-doping process was observed in the CV spectra, the LUMO levels were estimated from the HOMO

levels and the value of E_g determined from the UV-vis absorption spectrum using the equation:

$$LUMO = (HOMO + E_g)\ (eV)$$

The LUMO level was determined as -3.42 eV for TTVTPA and -3.49 eV for TTVCz. Conjugated molecules should have a high LUMO level for efficient charge dissociation in the BHJ type OSC. Note that the LUMO difference between the SSMs and $PC_{71}BM$ (~ -4.2 eV) is approximately 0.70 eV, i.e., there is a sufficient driving force to dissociate the exciton at the BHJ interface. Clearly, the electrochemical properties of these SSMs can be tuned by incorporating conjugated branches with different electron-donating groups (*t*TPA and *t*Cz) as the terminated moieties.

3.4 Thermal and optical properties of the SSM/$PC_{61}BM$ blends

The thermal properties of the TTVTPA/$PC_{61}BM$ and TTVCz/$PC_{61}BM$ blends were studied by using DSC. The results indicated that T_g values of the SSMs were decreased significantly by the incorporation of the $PC_{61}BM$ units, especially for the TTVCz/$PC_{61}BM$ blends (Table 2). This observation is attributed to the plasticizer effect of the $PC_{61}BM$. The incorporation of $PC_{61}BM$ enhanced the free volume between the SSMs and, thus, reduced the T_g of the TTVTPA/$PC_{61}BM$ and TTVCz/$PC_{61}BM$ blends. Nevertheless, the T_g values of the TTVTPA/$PC_{61}BM$ and TTVCz/$PC_{61}BM$ blends were slightly increased with the increase of the $PC_{61}BM$ content. This result implies that the presence of a large amount of $PC_{61}BM$ units resisted the molecular motion of the SSMs.

Figure 5 displays the normalized UV–vis absorption spectra of TTVTPA/$PC_{61}BM$ and TTVCz/$PC_{61}BM$ blends films prepared at various weight ratios. The absorption bands of the TTVTPA/$PC_{61}BM$ and TTVCz/$PC_{61}BM$ blends

extended from 375 to 800 nm. The maximal absorption peaks of the TTVTPA/$PC_{61}BM$ and TTVCz/$PC_{61}BM$ blends were observed at approximately 500 nm and 450 nm, respectively, while that of $PC_{61}BM$ ranged from 300 to 375 nm [41]. Moreover, the maximum absorption wavelength of the SSM/$PC_{61}BM$ blends increased with increasing amounts of $PC_{61}BM$. A red-shift of the absorption bands was observed for the TTVTPA/$PC_{61}BM$ and TTVCz/$PC_{61}BM$ blend films compared to that of the TTVTPA and TTVCz films. This result implies that the incorporation of $PC_{61}BM$ units reduced the aggregation of the conjugated molecules and favors the ICT between the triazine core and branches. However, for TTVTPA/$PC_{61}BM$ blends, the absorption band was blue-shifted as a higher amount of $PC_{61}BM$ (1:7, 1:9, w/w) was incorporated into the TTVTPA films. This behavior implies that the coplanarity of the triazine core and conjugated branches was disturbed as a large amount of $PC_{61}BM$ units was incorporated. The conformation of the SSM was strongly affected by the increased incorporation of the $PC_{61}BM$ units. In addition, the maximum absorption of the $PC_{61}BM$ sample appeared at ca. 330 nm [41]. The absorption intensity of the SSM/$PC_{61}BM$ blends decreased with increasing $PC_{61}BM$ content, which corresponds to the low absorption intensity of $PC_{61}BM$ in the visible absorption region.

The photoluminescence (PL) emission spectra of TTVTPA/$PC_{61}BM$ and TTVCz/$PC_{61}BM$ blends films prepared at various weight ratios are shown in Fig S2 (supporting information). TTVTPA and TTVCz exhibited PL maxima at *ca*. 700 nm upon excitation at 350 nm. The *t*TPA terminated TTVTPA exhibited a red-shift of the emission band relative to the *t*Cz terminated TTVCz due to the stronger electron-donating ability of *t*TPA group. The PL emission was almost completely quenched by the addition of $PC_{61}BM$ to TTVTPA and TTVCz (w/w =3:1). The completely quenching suggests that excitons generated by the absorbed photons

dissociated almost completely to become free charge carriers (electrons and holes). Thus, effective charge transfer from the p-type conjugated molecule to the electron acceptor $PC_{61}BM$ occurs — a basic requirement for preparing OSCs that exhibit satisfactory PV performance [42].

3.5 Morphology of the SSM/$PC_{61}BM$ blend films

The performance of the bulk heterojunction OSCs is strongly dependent on the morphology of the conjugated SSM/fullerene derivative composite film. To avoid recombination of the excitons, the P/N heterojunction phase must be controlled at the nanoscale level [43]. We used AFM microscopy to investigate the compatibility and morphology of our conjugated SSM/$PC_{61}BM$ composite films. Fig 6 displays the topographic and phase-contrast images of the TTVTPA/$PC_{61}BM$ blends films after annealing at 80 °C for 60 min. The surface roughness and thicknesses of the TTVTPA/$PC_{61}BM$ blends films are summarized in Table 2. In Fig 6(a), the phase image indicated that an obvious phase separation was observed for the TTVTPA/$PC_{61}BM$ (w/w = 1:1) blend film. The dark areas in the image represent $PC_{61}BM$ domains because the electron-scattering density of $PC_{61}BM$ is greater than that of the conjugated SSMs. The closer packing of triazine cored SSMs presumably reduced the compatibility between the TTVTPA and $PC_{61}BM$ in the film. From the topographic image (Fig 6(b)), we observed that the phase separation resulted in the high surface roughness of the TTVTPA/$PC_{61}BM$ (w/w = 1:1) blend film. As shown in Fig 6(c), the phase separation was improved for the TTVTPA/$PC_{61}BM$ (w/w = 1:3) blend film. The size of TTVTPA domains were reduced as the addition content of $PC_{61}BM$ was increased. Moreover, the surface roughness of the TTVTPA/$PC_{61}BM$ blend film was reduced significantly by the increase of the $PC_{61}BM$ content (Fig 6(d)). As the content of added $PC_{61}BM$ was further increased, the improvement of the compatibility between the TTVTPA and $PC_{61}BM$ in the film was sustained for the

TTVTPA/$PC_{61}BM$ (w/w = 1:5) blend film (Fig 6(e),(f)). A more homogeneous morphology was observed in the TTVTPA/$PC_{61}BM$ (w/w = 1:5) blend film in comparison with that of the TTVTPA/$PC_{61}BM$ (w/w = 1:3) blend film. For the TTVTPA/$PC_{61}BM$ (w/w = 1:7) blend film, we observed a phase-separated interpenetrating network with sizable $PC_{61}BM$ domains (Fig 6(g),(h)). Some degree of phase separation is critical for the efficient formation of free carriers to provide the optimal PV properties of OSCs. In addition, the distribution of the $PC_{61}BM$ units in the TTVTPA/$PC_{61}BM$ (w/w = 1:9) blend film (Fig 6(i) and (j)) was less uniform compared to that of the TTVTPA/$PC_{61}BM$ (w/w = 1:7) blend film (Fig 6(g) and (h)). The phase separation was obvious as an excess of $PC_{61}BM$ was incorporated into the TTVTPA/$PC_{61}BM$ (w/w = 1:9) blend film. The phase image revealed several $PC_{61}BM$ clusters (dark areas) in the TTVTPA/$PC_{61}BM$ blend film (Fig 6(i)). As a result, a higher surface roughness was observed for the TTVTPA/$PC_{61}BM$ blend film (Fig 6(j)). In addition, the topographic and phase-contrast images of the TTVCz/$PC_{61}BM$ blends films are shown in Fig 7. An obvious phase separation was observed for the TTVCz/$PC_{61}BM$ (w/w = 1:1) blend film, while a phase-separated interpenetrating network with sizable $PC_{61}BM$ domains was observed for the TTVCz/$PC_{61}BM$ (w/w = 1:3) blend film. A lower surface roughness was observed for the TTVCz/$PC_{61}BM$ (w/w = 1:3) blend film compared to that of the TTVCz/$PC_{61}BM$ (w/w = 1:1) blend film (Table 2). As shown in Fig 7(c), the $PC_{61}BM$ clusters were phase separated from the TTVCz/$PC_{61}BM$ (w/w = 1:5) blend film, which is accompanied with an increase of the surface roughness. The compatibility of TTVCz and $PC_{61}BM$ is different from that of TTVTPA and $PC_{61}BM$. The conjugated branches of SSMs with different terminal groups exhibited different stacking packing morphology, thereby resulting in the different compatibility with $PC_{61}BM$. To further characterize the distribution of $PC_{61}BM$ in the SSM/$PC_{61}BM$

films, a TEM investigation was performed. Bright-field TEM images of TTVTPA/PC61BM (w/w =1:7) and TTVCz/PC61BM (w/w =1:5) are shown in Fig 8. The dark areas in the images represent $PC_{61}BM$ domains because the electron-scattering density of $PC_{61}BM$ is greater than that of the SSM. The $PC_{61}BM$ unit was found to be uniformly distributed in the blend film after being annealed at 80°C for 1 h.

3.6 PV properties of the OSCs based on the SSM/$PC_{61}BM$ blend films

We fabricated OSCs incorporating a photoactive layer of the SSM/$PC_{61}BM$ blend film prepared by means of an optimized spin-coating procedure. Fig. 9 shows the photocurrent density–voltage plots of the OSCs. Table 2 summarizes the PV properties of these OSCs, including V_{OC}, short-circuit current density (J_{SC}), fill factor (FF), and PCE values. For the TTVTPA/$PC_{61}BM$-based OSCs (OSC I-1 – OSC I-5), the V_{OC} value was increased with increasing $PC_{61}BM$ content. The V_{OC} value of OSC I-1 was much lower than those of the other OSCs (OSC I-2 – OSC I-5). Although the value of V_{OC} is determined primarily by the difference between the LUMO energy level of the electron acceptor (in this case, $PC_{61}BM$) and the HOMO energy level of the electron donor (the conjugated SSM), it is also affected by the morphology of the photoactive layer [43-44]. As shown in Fig. S2a, the PL emission was not completely quenched for the TTVTPA/$PC_{61}BM$ (w/w = 1:1) blend film. This incomplete quenching indicated that the excitons generated by the absorbed photons were not dissociated to free charge carriers (electrons and holes). Moreover, AFM images indicated that the phase-separated interpenetrating networks with sizable domains were not formed in the photoactive layer for the TTVTPA/$PC_{61}BM$ (w/w = 1:1) blend film (Fig. 6(a)). The effective charge transfer from the p-type conjugated TTVTPA to the electron acceptor $PC_{61}BM$ was limited. As a result, the electron-hole recombination occurred at the interface of TTVTPA- and

$PC_{61}BM$-based domains and resulted in the low V_{OC} value of OSC I-1. However, the J_{SC}, FF, and PCE values of OSCs increased upon increasing the $PC_{61}BM$ content. The highest J_{SC}, FF, and PCE values were observed for the OSC I-5. This result indicates that the optimal composition of TTVTPA and $PC_{61}BM$ was approximately 1:7 (w/w) for the TTVTPA based OSCs. Higher concentrations of $PC_{61}BM$ favored the formation of phase-separated interpenetrating networks with sizable domains in the photoactive layer, which in turn led to an effective charge separation and charge transfer [45]. An efficient dissociation of the exciton and higher charge collection to the electrode are favorable for the enhancement of the OSCs. The hole mobilities of the SSM/$PC_{61}BM$ blend films were measured by the space-charge limited current method with a typical hole-only device structure of ITO/PEODT/SSM:$PC_{61}BM$/Au [26, 46-49]. The results are plotted as current density (J) vs. voltage (V), as shown in Fig. 10. The hole mobilities of the blend films are summarized in Table 2. The hole mobilities of the TTVTPA/$PC_{61}BM$ blend films were increased upon increasing the $PC_{61}BM$ content (Table 2). The hole mobilities of the TTVTPA/$PC_{61}BM$ blend films are in the range from 5.9×10^{-6} – 2.2×10^{-5} $cm^2/V.s$. The highest hole mobility (2.2×10^{-5} $cm^2/V.s$) was observed for the OSC I-4. According to the literature, the electron-mobility of PCBM is 4000 times higher than the hole mobility in the pure conjugated polymer [50,51]. Moreover, the ratio between the electron mobility and hole mobility is only a factor of ten in the polymer/PCBM blend film, resulting in a more balanced charge transport [52]. The hole mobility and charge balance seems to be enhanced by incorporation of $PC_{61}BM$ into the polymer composite [53]. However, excessive incorporation of the $PC_{61}BM$ content was not favorable for the charge transfer and the PV performance of the OSCs. OSC I-5 exhibited poorer hole-mobility and PV performance than those of OSC I-4. The micro-phase separation and aggregation of $PC_{61}BM$ resulted in charge recombination and current

leakage, which decreased the J_{SC} and PCE values for OSC I-5.

In addition, the V_{OC}, J_{SC}, FF, and PCE values of the TTVCz/$PC_{61}BM$ blend film based OSCs (OSC II-1 – OSC II-3) increased upon increasing the $PC_{61}BM$ content. The highest J_{SC} and PCE values were observed for the OSC II-2, which is due to the fact of that the optimal composition of TTVCz and $PC_{61}BM$ was about 1:3 (w/w) for the TTVCz based OSCs. In addition to the efficient solar light absorption, the PV performance was closely related to the charge transfer ability of the SSM/$PC_{61}BM$ blend film. The phase-separated interpenetrating networks with sizable domains in the photoactive layer were formed for the TTVCz/$PC_{61}BM$ (w/w = 1:3) blend film, which led to the improved hole-mobility (1.6×10^{-5} $cm^2/V.s$) and higher PV performance of OSC II-2. In addition, the values of V_{OC} of the TTVCz/$PC_{61}BM$ based OSCs (OSC II-1 – OSC II-3) were larger than those of the TTVTPA/$PC_{61}BM$ based OSCs (OSC I-1 – OSC I-5), presumably because of the lower HOMO level of TTVCZ compared to that of TTVTPA. In contrast, TTVTPA/$PC_{61}BM$ based OSCs exhibit the larger values of hole-mobility, J_{SC}, FF, and PCE than those of the TTVCz/$PC_{61}BM$ based OSCs. We attribute the improved charge mobility and PV performance of TTVTPA/$PC_{61}BM$-based OSCs to the improved conjugation of the *t*TPA group terminated TTVTPA.

In addition, the current density versus voltage curves indicates that the series resistance (R_S) is high and the shunt resistance (R_{SH}) is low (Fig. 9). The R_S and R_{SH} values of OSCs are summarized in Table 2. The R_S and R_{SH} values of BHJ type OSCs are closely related to the morphology of the SSM/$PC_{61}BM$ blend based photo-active layer and the quality of the interfacial contact between the SSM/$PC_{61}BM$ blend layer and the cathode [54-56]. The R_S values of the OSCs were decreased with increasing $PC_{61}BM$ content. The lowest R_S value was observed for the OSC I-4 based on the TTVTPA/$PC_{61}BM$ (1:7, w/w) blend. The phase-separated

interpenetrating networks with sizable domains in the photoactive layer allow for more efficient intra- and inter-molecular charge transport through the conjugated SSMs in the TTVTPA/$PC_{61}BM$ blend layer. Consequently, a lower R_S value was observed for the OSC I-4 [54,55] The influence of the $PC_{61}BM$ content on the TTVCz/$PC_{61}BM$ blend based OSCs (OSC II-1 – OSC II-3) is similar to those of the TTVTPA/$PC_{61}BM$ blend based OSCs (OSC I-1 – OSC I-5). OSC II-2 exhibited a lower R_S value than those of OSC II-1 and OSC II-3. In addition, a low R_{SH} value of the OSC was observed due to the poor contact between the photoactive layer and cathode. Poor contact between the photoactive layer and the cathode caused an increase in the charge recombination and leakage current, which resulted in the low R_{SH} value of OSC [55,56]. The R_{SH} values of the OSCs were decreased with increasing $PC_{61}BM$ content, which is attributed to the decrease of the surface roughness value of the SSM/$PC_{61}BM$ blend films. A lower surface roughness led to the poor interfacial contact between the photo-active layer and cathode. As a result, lower R_{SH} values were observed for the OSC I-4 and OSC II-2 compared to those of the other OSCs. Nevertheless, the PV performance of OSCs was enhanced with an increase of the $PC_{61}BM$ content in the photoactive layer.

3.7 PV properties of the OSCs based on the SSM/$PC_{71}BM$ blend films

To further improve the PV performance of TTVTPA- and TTVCz-based OSCs, $PC_{71}BM$ was introduced instead of $PC_{61}BM$ as the electron-acceptor in the photo-active layer of the OSCs. Photocurrent density–voltage plots of the SSM/$PC_{71}BM$ blend film based OSCs (OSC III-1 and OSC III-2) are shown in Fig. 9. The PV properties of these OSCs are summarized in Table 2. Because the optimal composition of the TTVTPA/$PC_{61}BM$ and TTVCz/$PC_{61}BM$ blends are 1:7 and 1:3 (w/w), respectively, the OSC III-1 and OSC III-2 based on TTVTPA/$PC_{71}BM$ and TTVCz/$PC_{71}BM$ blends with compositions of 1:7 and 1:3 (w/w) were studied.

Indeed, AFM images indicated that phase-separated interpenetrating networks with sizable domains in the photoactive layer were formed for the TTVTPA/$PC_{71}BM$ and TTVCz/$PC_{71}BM$ blend films (Fig. S3, supporting information). Moreover, TEM images indicated that the $PC_{71}BM$ units are distributed uniformly in the TTVTPA/$PC_{71}BM$ and TTVCz/$PC_{71}BM$ blend films (Fig S4, supporting information). OSC III-1 fabricated from the TTVTPA/$PC_{71}BM$ blend (w/w = 1:7) film exhibited a hole-mobility of 2.7 x 10^{-5} cm^2/V.s, a V_{OC} of 0.69 V, a J_{SC} of 10.57 mA/cm^2, a FF of 0.34, and a PCE of 2.48%. The TTVCz/$PC_{71}BM$ blend (w/w = 1:3) film based OSC III-2 exhibited a hole-mobility of 1.8 x 10^{-5} cm^2/V.s, a V_{OC} of 0.78 V, a J_{SC} of 6.0 mA/cm^2, a FF of 0.31, and a PCE of 1.45%. The R_S values of OSC III-1 and OSC III-2 are 36.5 and 81.1 $k\Omega cm^2$, respectively, while the R_{SH} values are 0.16 and 0.71 $k\Omega cm^2$, respectively. Much higher J_{SC} and PCE values were observed for the SSM/$PC_{71}BM$ blend film based OSCs compared to those of the SSM/$PC_{61}BM$ blend film based OSCs. This difference was because of the stronger and broader absorption of $PC_{71}BM$ in the visible region [57]. In addition, the J_{SC} and PCE values of the A-π-D structured SSMs (TTVTPA and TTVCz) based OSCs are comparable to those of the literature reported D-π-A and D-A-D structured SSM based OSCs, even though the triazine cored SSMs (TTVTPA and TTVCz) exhibited shorter absorption wavelengths than the TPA cored SSMs [19, 22-24, 29]. This result implies that the charge generation and transporting capacity of the A-π-D structured SSM based OSC were comparable to those of the D-π-A or D-A-D structured SSM based OSC. The convergence of dipole moments from the peripheral groups to the central core along the conjugated branches is beneficial to the charge transport from the SSM to the fullerene derivative.

Conclusion

Two new A-π-D structured SSMs (TTVTPA and TTVCz) were developed for application as donor materials in solution processed BHJ type OSCs. The incorporation of the electron deficient triazine group as the core decreases the LUMO level and energy gap of the SSMs. The red-shift of the absorption band for TTVTPA relative to TTVCz is due to the stronger electron-donating character and more efficient π-π* charge transfer of tTPA terminated branches. This is favorable for harvesting large amounts of solar radiation. In addition to the efficient solar light absorption, the PV performance was closely related to the charge transfer ability of the SSM/fullerene derivative blend film. TTVTPA/fullerene derivative based OSCs exhibit larger values of hole-mobility than do the TTVCz/fullerene derivative based OSCs. Consequently, the PV properties of the TTVTPA/fullerene derivative based OSCs were much better than those of the TTVCz/fullerene derivative blend based OSCs. This study provided a new approach for the chemical design of star-shaped conjugated molecules for OSC application.

Acknowledgment

The authors thank the Ministry of Science and Technology, ROC, for their financial support (Grant NSC 101-2221-E-005-012-MY3).

References

1. J. You, L. Dou, K. Yoshimura, T. Kato, K. Ohya, T. Moriarty, K. Emery, C. Chen, J. Gao, G. Li and Y. Yang, Nature Commun., 2013, 4, 1446.
2. J. Roncali, P. Frere, P. Blanchard, R. de Bettignies, M. Turbiez, S. Roquet, P. Leriche and Y. Nicolas, Thin Solid Films, 2006, 511-512, 567.
3. Y. Liu, J. Zhou, X. Wan and Y. Chen, Tetrahedron, 2009, 65, 5209.

4. W. Zhang, S. C. Tse, J. Lu, Y. Tao and M. S. Wong, J. Mater. Chem., 2010, 20, 2182.
5. T. S. van der Poll, J. A. Love, T. Q. Nguyen and G. C. Bazan, Adv. Mater., 2012, 24, 3646.
6. J. Zhou, X. Wan, Y. Liu, Y. Zuo, Z. Li, G. He, G. Long, W. Ni, C. Li, X. Su and Y. Chen, J. Am. Chem. Soc., 2012, 134, 16345.
7. Y. Sun, G. C. Welch, W. L. Leong, C. J. Takacs, G. C. Bazan and A. J. Heeger, Nature Mater., 2012, 11, 44.
8. Z. Li, G. He, X. Wan, Y. Liu, J. Zhou, G. Long, Y. Zuo, M. Zhang and Y. Chen, Adv. Energy Mater., 2012, 2, 74.
9. J. Roncali, Acc. Chem. Res., 2009, 42, 1719.
10. S. Shen, P. Jiang, C. He, J. Zhang, P. Shen, Y. Zhang, Y. Yi, Z. Zhang, Z. Li and Y. Li, Chem. Mater., 2013, 25, 2274.
11. C. A. Echeverry, A. Insuasty, M. A. Herranz, A. Ortiz, R. Cotta, V. Dhas, L. Echegoyen, B. Insuasty and N. Martin, Dyes Pigm., 2014, 107, 9.
12. S. Roquet, R. de Bettignies, P. Leriche, A. Cravino and J. Roncali, J. Mater. Chem., 2006, 16, 3040.
13. N. Kopidakis, W. J. Mitchell, J. Van de Lagemaat, D. S. Ginley, G. Rumbles, S. E. Shaheen and W. L. Rance, Appl. Phys. Lett., 2006, 89, 103524.
14. W. Zhang, G. M. Ng, H. L. Tam, M. S. Wong and F. Zhu, J. Polym. Sci.: Polym. Chem. A, 2011, 49, 1865.
15. H. C. Hesse, J. Weickert, M. Al-Hussein, L. Dossel, X. Feng, K. Mullen and L. Schmidt-Mende, Sol. Energy Mater. Sol. Cells, 2010, 94, 560.
16. S. Roquet, A. Cravino, P. Leriche, O. Aleveque, P. Frere and J. Roncali, J. Am. Chem. Soc., 2006, 128, 3459.

17. E. Ripaud, Y. Olivier, P. Leriche, J. Cornil and J. Roncali, J. Phys. Chem. B, 2011, 115, 9379.

18. H. M. Ko, H. Choi, S. Paek, K. Kim, K. Song, J. K. Lee and J. Ko, J. Mater. Chem., 2011, 21, 7248.

19. D. Deng, S. Shen, J. Zhang, C. He, Z. Zhang and Y. Li, Org. Electron., 2012, 13, 2546-2552.

20. J. Min, Y. N. Luponosov, T. Ameri, A. Elschner, S. M. Peregudove, D. Baran, T. Heumuller, N. Li, F. Machui, S. Ponomarenko and C. J. Brabec, Org. Electron., 2013, 14, 219.

21. E. Ripaud, T. Rousseau, P. Leriche and J. Roncali, Adv. Energy Mater., 2011, 1, 540.

22. J. Zhang, D. Deng, C. He, Y. He, M. Zhang, Z. G. Zhang, Z. Zhang and Y. Li, Chem. Mater., 2011, 23, 817.

23. Y. Jiang, D. Yu, L. Lu, C. Zhqan, D. Wu, W. You, Z. Xie and S. Xiao, J. Mater. Chem. A, 2013, 1, 8270.

24. J. Zhang, J. Yu, C. He, D. Deng, Z. G. Zhang, M. Zhang, Z. Li and Y. Li, Org. Electron., 2012, 13, 166.

25. D. Sahu, C. H. Tsai, H. Y. Wei, K. C. Ho, F. C. Chang and C. W. Chu, J. Mater. Chem., 2012, 22, 7945.

26. A. Tang, L. Li, Z. Lu, J. Huang, H. Jia, C. Zhan, Z. Tan, Y. Li and J. Yao, J. Mater. Chem. A, 2013, 1, 5747.

27. H. Shang, H. Fan, Y. Liu, W. Hu, Y. Li and X. Zhan, Adv. Mater., 2011, 23, 1554.

28. Y. Nicolas, P. Blanchard, E. Levillain, M. Allain, N. Mercier, J. Roncali, Org. Lett., 2004, 6, 273-276.

29. R. de Bettignies, Y. Nicolas, P. Blanchard, E. Levillain, J. M. Nunzi and J. Roncali, Adv. Mater., 2003, 15, 1939.

30. Z. Lu, C. Li, T. Fang, G. Li and Z. Bo, J. Mater. Chem. A, 2013, 1, 7657.
31. T. A. Liu, C. Prabhakar, J. Y. Yu, C. H. Chen, H. H. Huang and J. S. Yang, Macromolecules, 2012, 45, 4529.
32. C. He, Q. He, Y. Yi, G. Wu, F. Bai, Z. Shuai and Y. Li, J. Mater. Chem., 2008, 18, 4085.
33. J. Zhang, Y. Yang, C. He, Y. He, G. Zhao and Y. Li, Macromolecules, 2009, 42, 7619.
34. G. Wu, G. Zhao, C. He, J. Zhang, Q. He, X. Chen, Y. Li, Sol. Energy Mater. Sol. Cells, 2009, 93, 108.
35. H. J. Wang, J. Y. Tzeng, C. W. Chou, C. Y. Huang, R. H. Lee and R. J. Jeng, Polym. Chem., 2013, 4, 506.
36. R. H. Lee, W. S. Chen and Y. Y. Wang, Thin Solid Films, 2009, 517, 5747.
37. G. S. Liou, S. H. Hsiao and H. W. Chen, J. Mater. Chem., 2006, 16, 1831.
38. H. M. Wang, S. H. Hsiao, G. S. Liou and C. H. Sun, J. Polym. Sci., Part A: Polym. Chem., 2010, 48, 4775.
39. O. Kwon, S. Barlow, S. A. Odom, L. Beverina, N. J. Thompson, E. Zojer, J. L. Br´edas and S. R. Marder, J. Phys. Chem. A, 2005, 109, 9346.
40. M. C. Scharber, D. Wuhlbacher, M. Koppe, P. Denk, C. Waldauf, A. J. Heeger and C. L. Brabec, Adv. Mater., 2006, 18, 789.
41. R. H. Lee and L. W. Liu, Dyes Pigm., 2010, 84, 190.
42. A. Mishra and P. Bauerle, Angew. Chem. Int. Ed., 2012, 51, 2020.
43. A. Gadisa, M. Svensson, M. R. Andersson and O. Inganas, Appl. Phys. Lett. 2004, 84, 1609.

44. K. Vandewal, A. Gadisa, W. D. Oosterbaan, S. Bertho, F. Banishoeib, I. V. Severen, L. Lutsen, T. J. Cleij, D. Vanderzande and J. V. Manca, Adv. Funct. Mater., 2008, 18, 2064.

45. R. H. Lee and L. Y. Lee, Colloid. Polym. Sci., 2011, 289, 1215.

46. Y. Liu, X. Wan, F. Wang, J. Zhou, G. Long, J. Tian and Y. Chen, Adv. Mater. 2011, 23, 5387.

47. C. Goh, R. J. Kline, M. D. McGehee, E. N. Kadnikova and J. M. J. Frechet, App. Phys. Lett., 2005, 86, 122110.

48. G. D. Sharma, P. Suresh, S. S. Sharma, Y. K. Vijay and J. A. Mikroyannidis, ACS Appl. Mater. Interface, 2010, 2, 504.

49. H. Zhou, L. Yang, S. Stoneking and W. You, ACS Appl. Mater. Interfaces, 2, 2010, 1377.

50. V. D. Mihailetchi, J. K. J. van Duren, P. W. M. Blom, J. C. Hummelen, R. A. J. Janssen, J. M. Kroon, M. T. Rispens, W. J. H. Verhees and M. M. Wienk, Adv. Funct. Mater., 2003, 13, 43.

51. P. W. M. Blom, M. J. M. D. Jong and M. J. van Munster, Phys. Rev. B, 1997, 55, R656.

52. C. Melzer, E. Koop, V. D. Mihailetchi and P. W. M. Blom, Adv. Funct. Mater., 2004, 14, 865.

53. V. D. Mihailetchi, L. J. A. Koster, P. W. M. Blom, C. Melzer, B. D. Boer, J. K. J. V. Duren and R. A. J. Janssen, Adv. Funct. Mater., 2005, 15, 795.

54. H. Sirringhaus, P. J. Brown, R. H. Friend, M. M. Nielsen, K. Bechgaard, B. M. W. Langeveld-Voss, A. J. H. Spiering, R. A. J. Janssen, E. W. Meijer, P. Herwig, and D. M. Leeuw, Nature 1999, 401, 685.

55. M. S. Kim, B. G. Kim and J. Kim, ACS Appl. Mater. Interfaces 2009, 1, 1264.

56. F. C. Grozema, P. T. van Duijnen, Y. A. Berlin, M. A. Ratner and L. D. A. Siebbeles, J. Phys. Chem. B, 2002, 106, 7791.

57. H. J. Wang, L. H. Chan, C. P. Chen, S. L. Lin, R. H. Lee and R. J. Jeng, Polymer, 2011, 52, 326.

Figure Captions

Table 1. Optical properties, electrochemical onset potentials, and electronic energy levels of the TTVTPA and TTVCz.

Table 2. Photovoltaic performances of the OSCs based on SSM/fullerene derivative photoactive layers.

Scheme 1. Synthesis routes of the compounds 1, 3, 5, and 7.

Scheme 2. Synthesis routes of the triazine cored star-shaped molecules TTVTPA and TTVCz.

Fig 1. Illustrations of D-π-A and A-π-D structured SSMs.

Fig 2. Illustrations of the charge transfer from the SSM to the fullerene derivatives in the photoactive layer.

Fig 3. UV-vis absorption spectra of TTVTPA and TTVCz in solution and in thin-film states.

Fig 4. Cyclic voltammograms of TTVTPA and TTVCz.

Fig. 5. Normalized UV-vis absorption spectra of (a) TTVTPA/$PC_{61}BM$ and (b) TTVCz/$PC_{61}BM$ blend films.

Fig. 6. AFM tapping mode phase (a, c, e, g, i) and topographic (b, d, f, h, j) images of TTVTPA/$PC_{61}BM$ blend films (a, b: w/w=1:1; c, d: w/w=1:3; e, f: w/w=1:5; g, h: w/w=1:7; i, j: w/w=1:9) after annealing at 80 °C for 60 min.

Fig 7. AFM tapping mode phase (a, b, c) and topographic (d, e, f) images of TTVCz/$PC_{61}BM$ blend films (a, d: w/w=1:1; b, e: w/w=1:3; c, f: w/w=1:5) after annealing at 80 °C for 60 min.

Fig 8. TEM images of (a) TTVTPA/$PC_{61}BM$ (w/w = 1:7) and (b) TTVCz/$PC_{61}BM$ (w/w = 1:3) blend films after annealing at 80 °C for 60 min.

Fig 9. Current density-potential characteristics of illuminated (AM 1.5 G, 100 mW/cm^2) SSM/$PC_{61}BM$- and SSM/$PC_{71}BM$-based solar cells.

Fig 10. Plots of $(J)^{0.5}$ vs. V of SSM/PC_{61}BM- and SSM/PC_{71}BM-based hole-only devices.

Table 1. Optical properties, electrochemical onset potentials, and electronic energy levels of the TTVTPA and TTVCz.

Molecule	λ_{max}^{abs} (nm)[§]	λ_{max}^{abs} (nm)*	λ_{onset}^{abs} (nm)[ζ]	E_g^{opt} (eV)[#]	E_{on}^{ox} (V)	HOMO (eV)	LUMO (eV)
TTVTPA	495	488	605	2.05	0.76	-5.47	-3.42
TTVCZ	442	446	595	2.09	0.87	-5.58	-3.49

§ Maximal absorption wavelength of the star-shaped molecules in solution. * Maximal absorption wavelength of the star-shaped molecule as thin film. ζ The onset of UV-vis absorption of the star-shaped molecule as thin film. # Calculated E_g from the onset absorption (λ_{onset}^{abs}) of the star-shaped molecule based thin film: $E_g = 1240/\lambda_{onset}$.

Table 2. Photovoltaic performances of the OSCs based on SSM/fullerene derivative photoactive layers.

OSC	Photoactive layer	SSM/ $PC_{61}BM$ (w/w)	T_g (°C)	*d* (nm)	*R* (nm)	V_{OC} (V)	J_{SC} (mA cm^{-2})	FF	PCE (%)	R_{SH} (kΩ cm^2)	R_S (kΩ cm^2)	Mobility (cm^2/V.s)
OSC I-1	TTVTPA/$PC_{61}BM$	1:1	110.1	85	0.83	0.56	1.06	0.33	0.20	1.02	287.9	5.9×10^{-6}
OSC I-2	TTVTPA/$PC_{61}BM$	1:3	119.3	84	0.33	0.62	1.36	0.35	0.30	0.92	219.1	8.9×10^{-6}
OSC I-3	TTVTPA/$PC_{61}BM$	1:5	123.2	80	0.30	0.62	3.75	0.35	0.81	0.47	84.7	1.4×10^{-5}
OSC I-4	TTVTPA/$PC_{61}BM$	1:7	130.7	81	0.29	0.68	4.80	0.36	1.18	0.49	68.6	2.2×10^{-5}
OSC I-5	TTVTPA/$PC_{61}BM$	1:9	133.4	78	0.31	0.69	3.41	0.36	0.85	0.55	81.4	1.5×10^{-5}
OSC II-1	TTVCz/$PC_{61}BM$	1:1	132.7	83	0.63	0.70	1.19	0.26	0.22	0.58	314.3	8.8×10^{-6}
OSC II-2	TTVCz/$PC_{61}BM$	1:3	133.9	81	0.33	0.77	3.82	0.32	0.93	0.38	109.8	1.6×10^{-5}
OSC II-3	TTVCz/$PC_{61}BM$	1:5	131.1	80	0.47	0.78	3.31	0.32	0.82	0.51	140.6	1.4×10^{-5}
OSC III-1	TTVTPA/$PC_{71}BM$	1:7	132.5	79	0.32	0.69	10.57	0.34	2.48	0.56	36.5	2.7×10^{-5}
OSC III-2	TTVCz /$PC_{71}BM$	1:3	135.6	80	0.36	0.78	6.00	0.31	1.45	0.71	81.1	1.8×10^{-5}

SSM: Star shaped molecule.

d: Thickness of the photo-active layer.

R: Roughness of the photo-active layer.

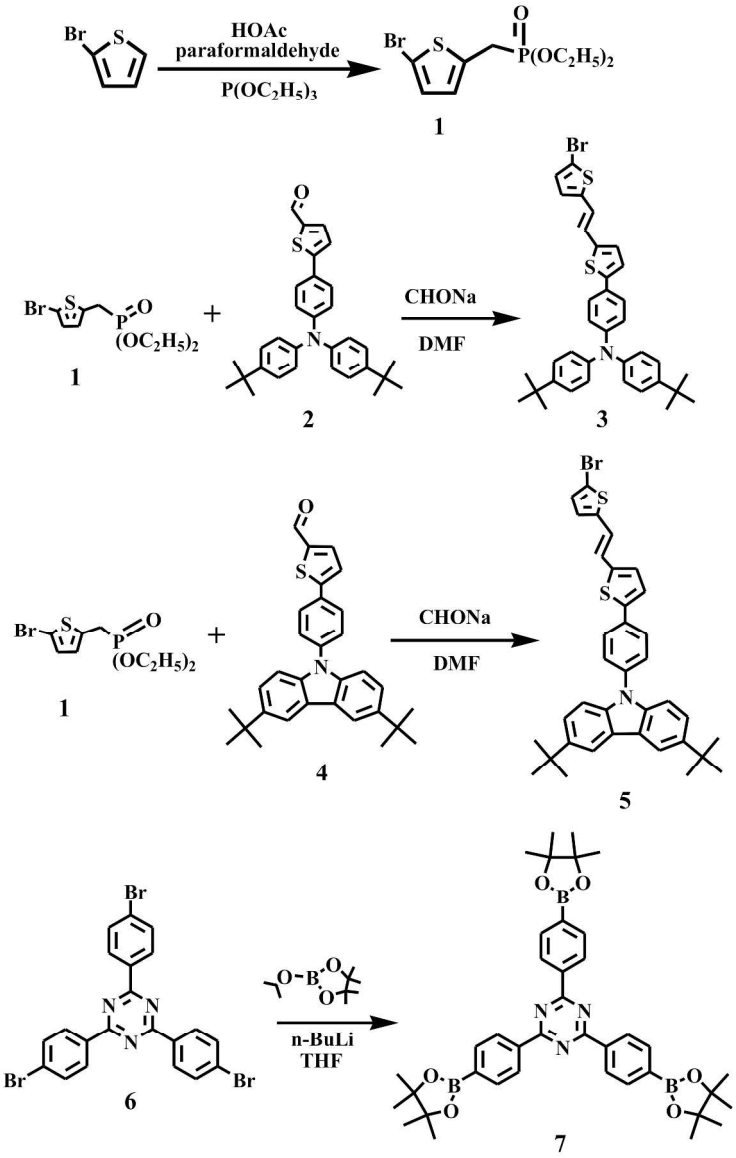

Synthesis routes of the compounds 1, 3, 5, and 7.
128x199mm (600 x 600 DPI)

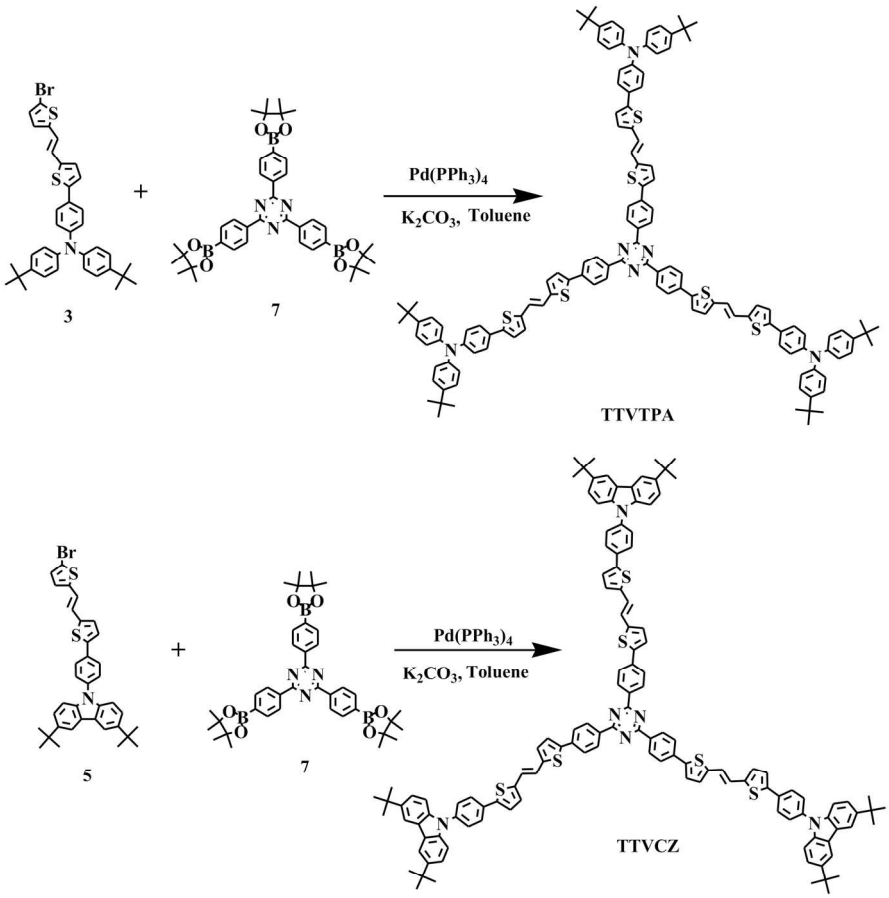

Synthesis routes of the triazine cored star-shaped molecules TTVTPA and TTVCz.
84x86mm (600 x 600 DPI)

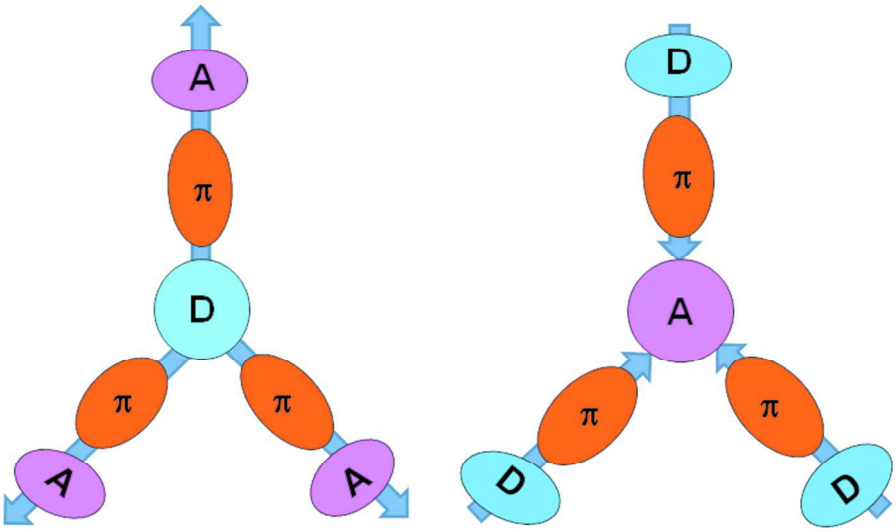

(a) D-π-A structured SSM (b) A-π-D structured SSM

Illustrations of D-∏-A and A-∏-D structured SSMs.
59x43mm (600 x 600 DPI)

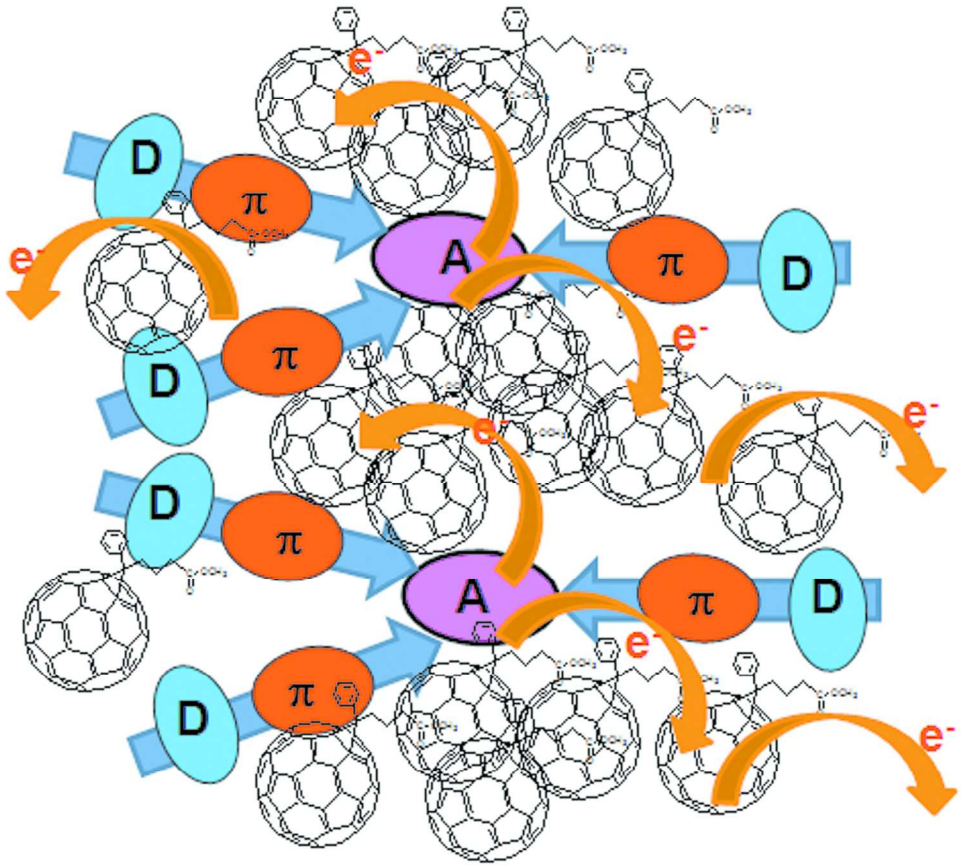

Illustrations of the charge transfer from the SSM to the fullerene derivatives in the photoactive layer.
71x61mm (600 x 600 DPI)

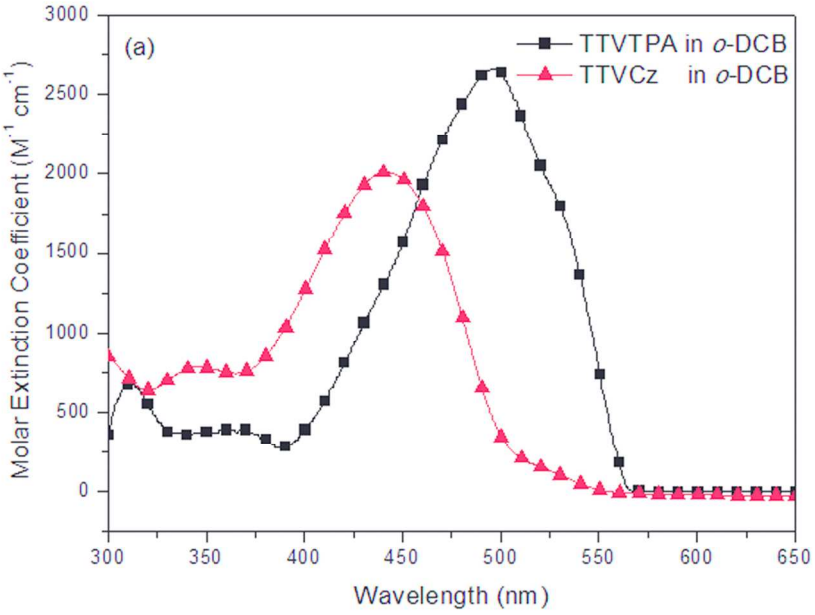

UV-vis absorption spectra of TTVTPA and TTVCz in solution and in thin-film states.
61x44mm (600 x 600 DPI)

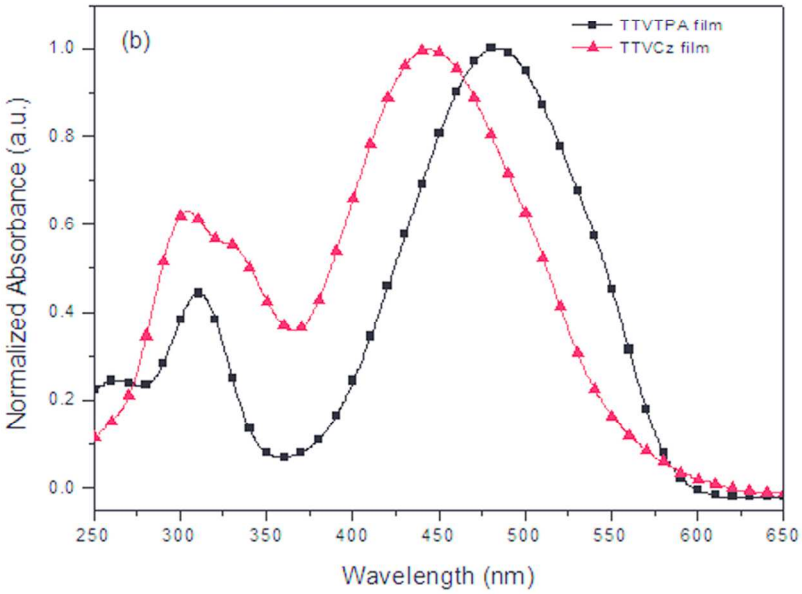

UV-vis absorption spectra of TTVTPA and TTVCz in solution and in thin-film states.
61x43mm (600 x 600 DPI)

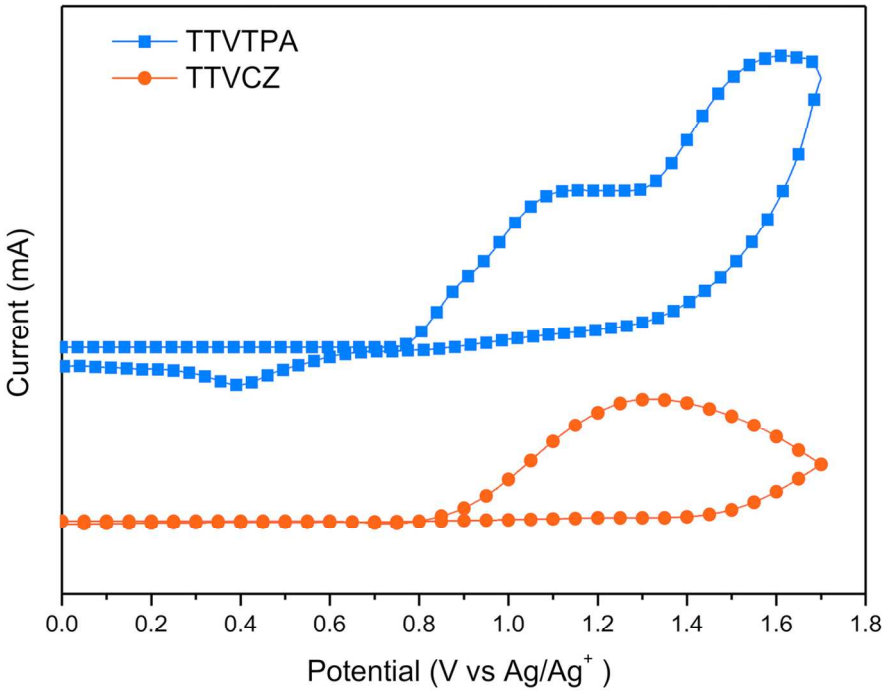

Cyclic voltammograms of TTVTPA and TTVCz.
65x52mm (600 x 600 DPI)

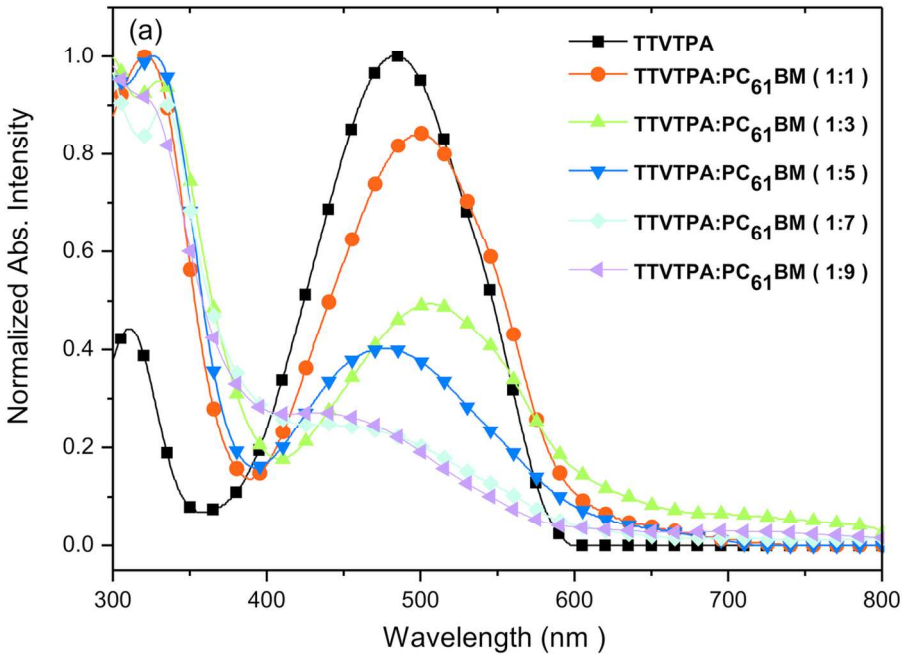

Normalized UV-vis absorption spectra of (a) TTVTPA/PC61BM and (b) TTVCz/PC61BM blend films.
62x47mm (600 x 600 DPI)

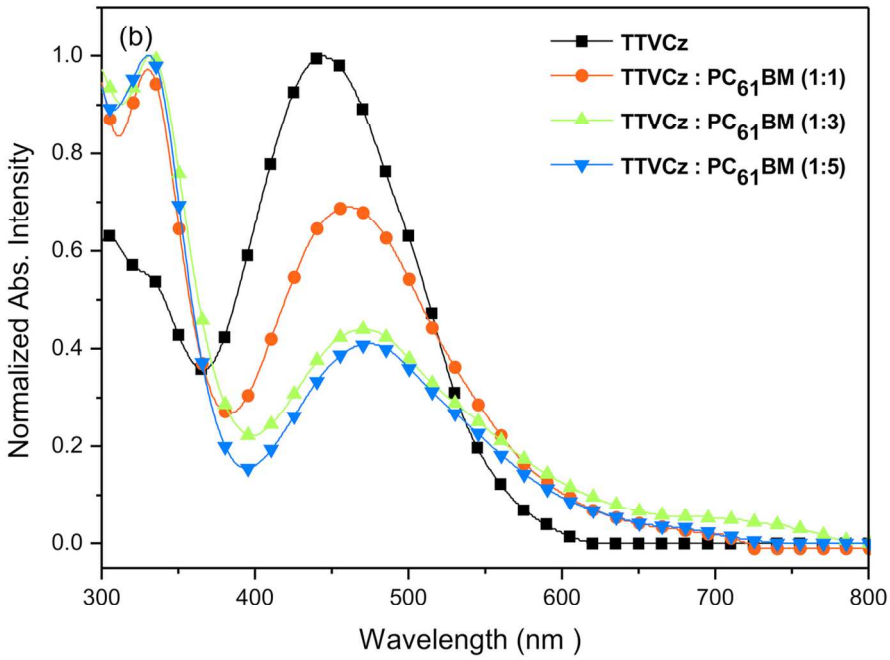

Normalized UV-vis absorption spectra of (a) TTVTPA/PC61BM and (b) TTVCz/PC61BM blend films.
63x49mm (600 x 600 DPI)

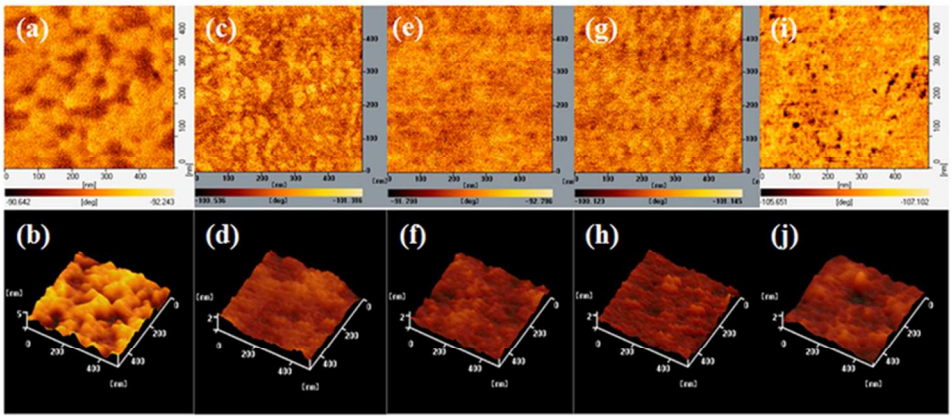

AFM tapping mode phase (a, c, e, g, i) and topographic (b, d, f, h, j) images of TTVTPA/PC61BM blend films (a, b: w/w=1:1; c, d: w/w=1:3; e, f: w/w=1:5; g, h: w/w=1:7; i, j: w/w=1:9) after annealing at 80 °C for 60 min.
34x16mm (600 x 600 DPI)

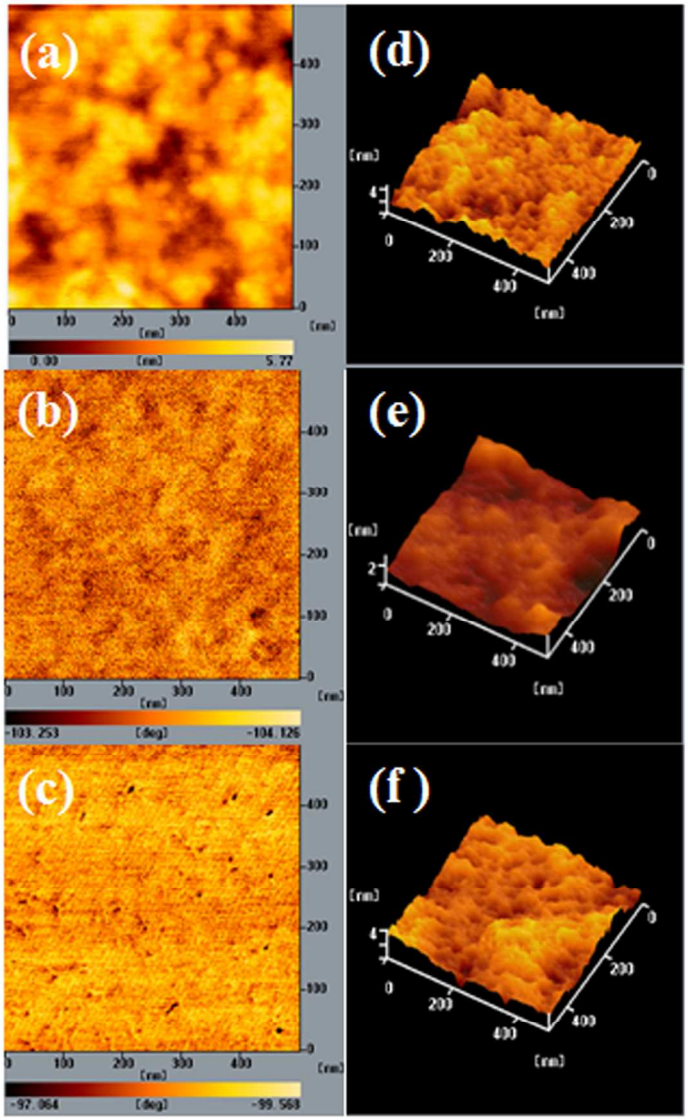

AFM tapping mode phase (a, b, c) and topographic (d, e, f) images of TTVCz/PC61BM blend films (a, d: w/w=1:1; b, e: w/w=1:3; c, f: w/w=1:5) after annealing at 80 °C for 60 min.
81x126mm (600 x 600 DPI)

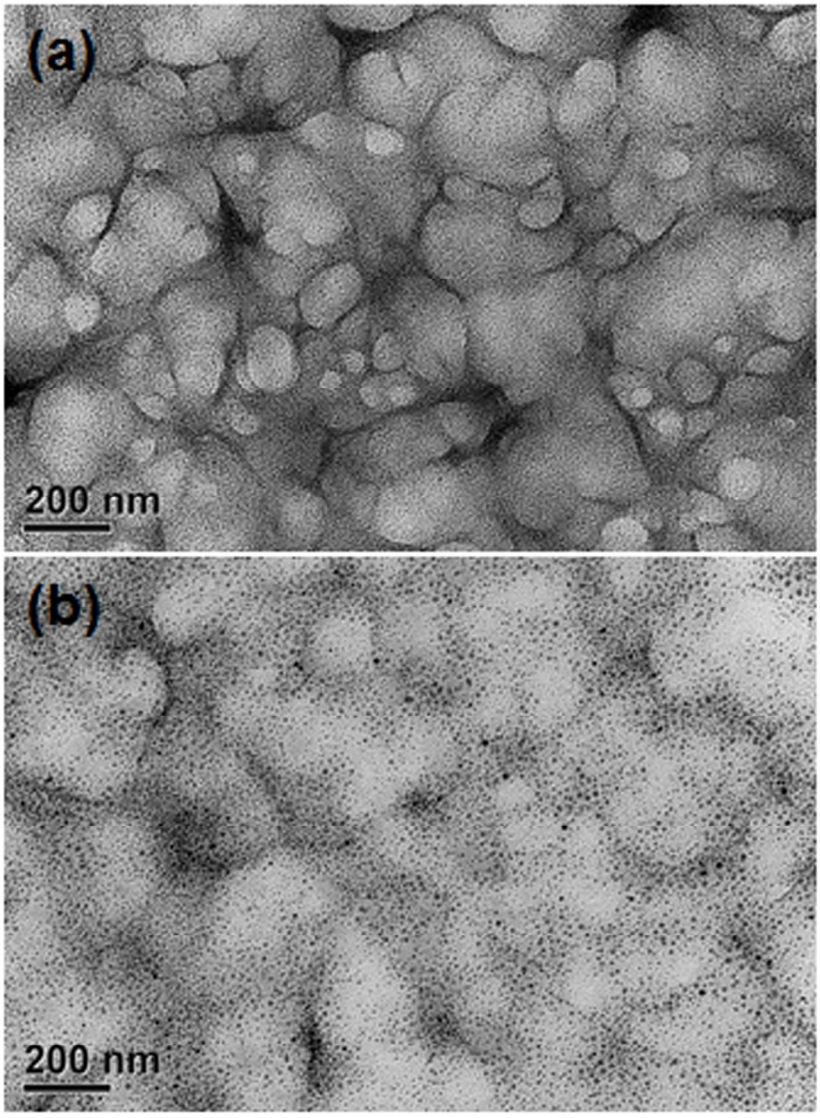

TEM images of (a) TTVTPA/PC61BM (w/w = 1:7) and (b) TTVCz/PC61BM (w/w = 1:3) blend films after annealing at 80 °C for 60 min.
69x91mm (600 x 600 DPI)

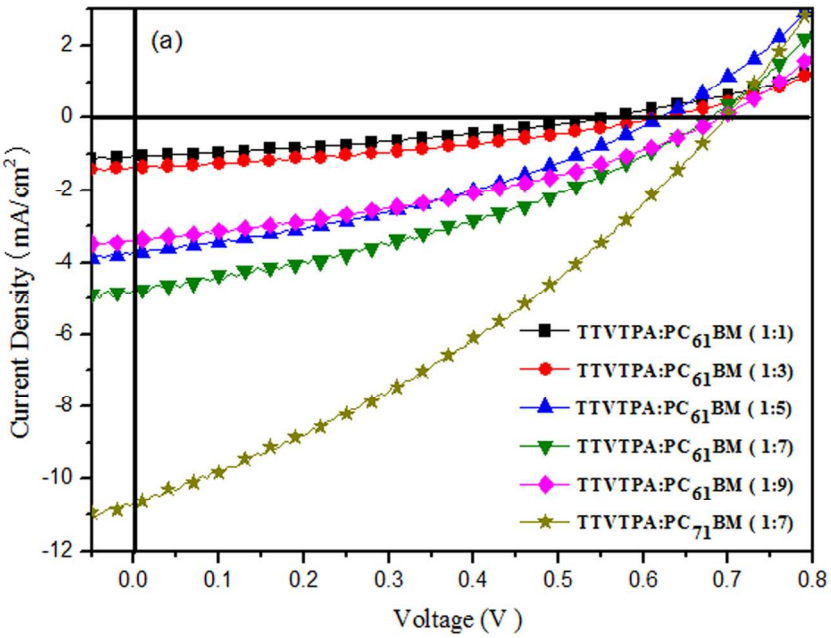

Current density-potential characteristics of illuminated (AM 1.5 G, 100 mW/cm2) SSM/PC61BM- and SSM/PC71BM-based solar cells.
68x56mm (600 x 600 DPI)

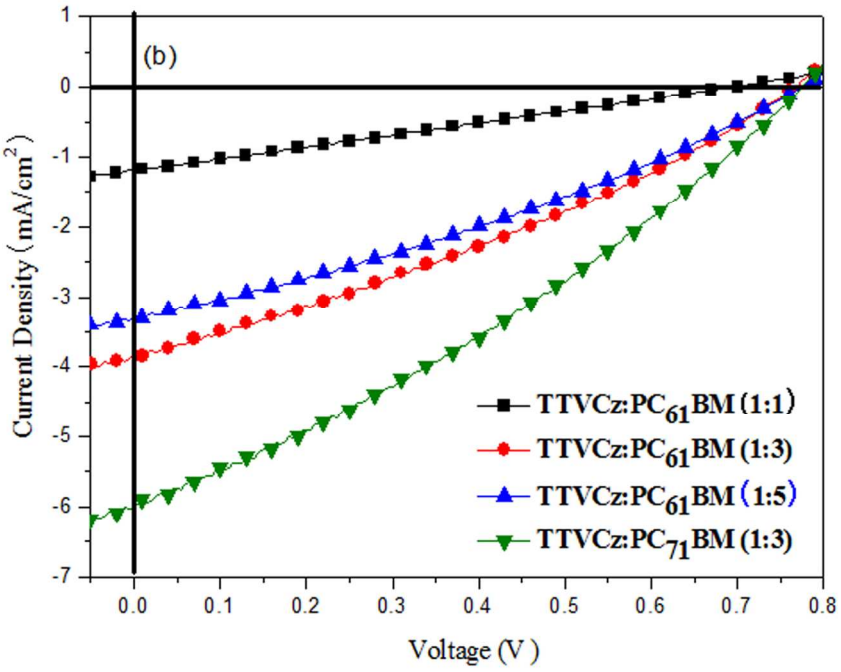

Current density-potential characteristics of illuminated (AM 1.5 G, 100 mW/cm2) SSM/PC61BM- and SSM/PC71BM-based solar cells.
69x58mm (600 x 600 DPI)

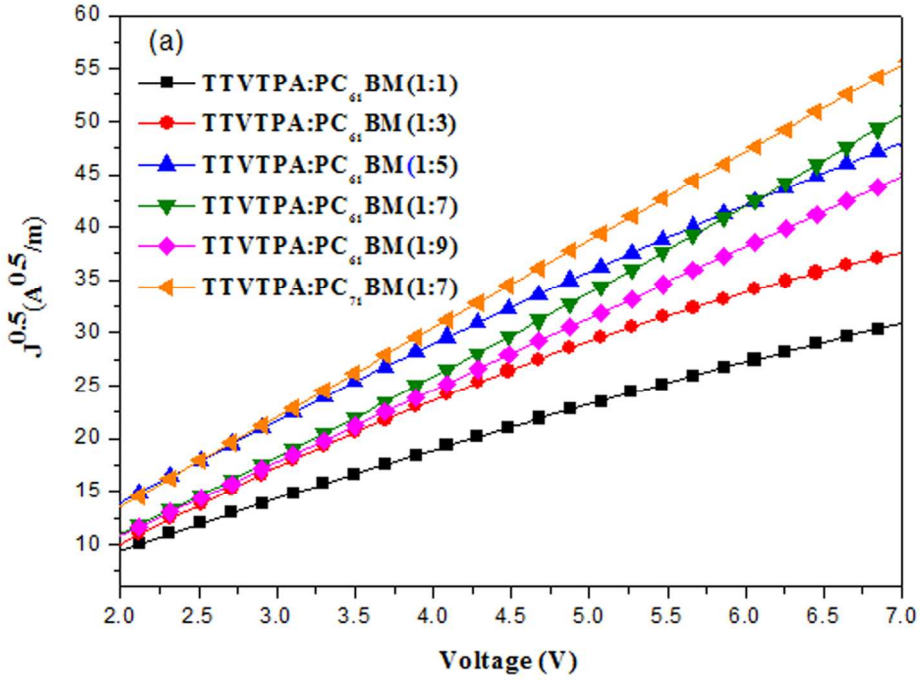

Plots of (J)0.5 vs. V of SSM/PC61BM- and SSM/PC71BM-based hole-only devices.
59x42mm (600 x 600 DPI)

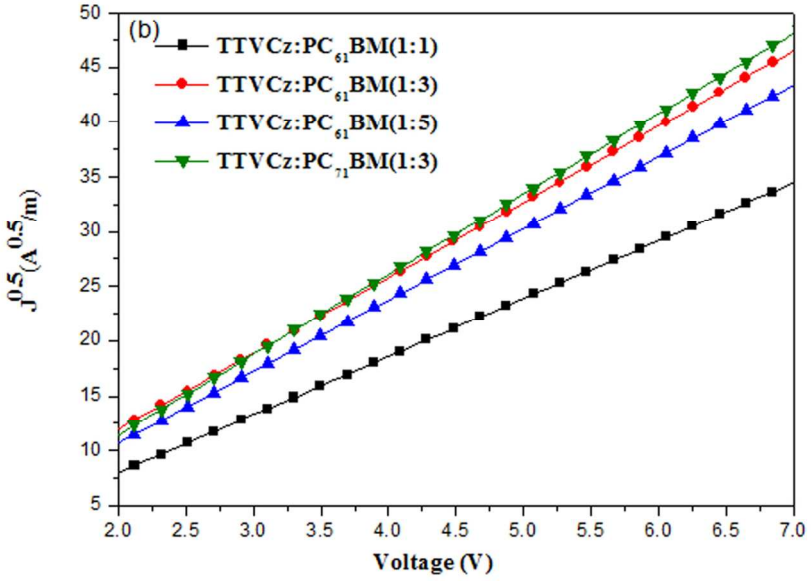

Plots of (J)0.5 vs. V of SSM/PC61BM- and SSM/PC71BM-based hole-only devices.
57x39mm (600 x 600 DPI)